



Interfacial engineering and configuration design of bilayered photoanode consisting of macroporous tin dioxide/titanium dioxide for high performance dye-sensitized solar cells



Peilu Zhao^a, Hongbin Sun^a, Liyuan Tian^a, Biao Wang^b, Fengmin Liu^{a,*}, Peng Sun^a, Geyu Lu^{a,*}

^a College of Electronic Science and Engineering, Jilin University, PR China

^b Changchun Institute of Optics, Fine Mechanics and Physics, PR China

ARTICLE INFO

Article history:

Received 13 May 2015

Received in revised form 24 June 2015

Accepted 18 July 2015

Available online 26 July 2015

Keywords:

Dye-sensitized solar cells
tin oxide/titanium oxide composite materials
double layered photoanode
slow electron recombination
light-harvesting efficiency

ABSTRACT

Two kinds of tin oxide (SnO₂)/titanium oxide (TiO₂) composite materials have been synthesized and applied as electrodes in dye-sensitized solar cells (DSSCs) with high performance. The porous SnO₂/TiO₂ material (PSTM) consisting of SnO₂ nanosheets cluster and TiO₂ nanoparticles (P25) shows a superior dye adsorption ability due to its large specific surface area (151.1 m² g⁻¹). The PSTM based cell exhibits the slowest electron recombination rate among the cells tested from electrochemical impedance spectra measurements, and obtains final power conversion efficiency (PCE) up to 6.80%. Another novel structure of SnO₂@TiO₂ hollow sphere (STHS) prepared via a facile water bath process is designed to improve the light utilization efficiency with its excellent light scattering ability. Though the charge recombination resistance of STHS (25.6 Ω) is smaller than that of P25 (30.6 Ω), the PCE of the DSSCs based on the former is 5.82%, showing over 9.2% increment than the latter (5.33%). This can be mainly ascribed to the enhanced light-harvesting ability and charge collection efficiency of the macroporous hollow sphere structure, both of which contribute to a higher short current density and hence for the better photovoltaic performance. Furthermore, we demonstrate a bilayered film of PSTM (charge conduction layer) and STHS (light scattering layer) as photoanode aiming to further improve the efficiency of DSSC by engineered integration of different promising materials. The results indicate that the PSTM+STHS based cell shows an obvious 14.6% increase of PCE (7.79% with a J_{sc} of 17.49 mA cm⁻², V_{oc} of 0.73 V and FF of 0.61) as compared to the single layered PSTM photoelectrode with the same thickness of ~6.9 μm, providing the specific evidence for taking full advantages of the superior dye adsorption, fast charge collection as well as strong light harvesting simultaneously. Fundamentally, this study not only provides a scheme for the guidance of effective materials surface and interfacial modification, but also highlights the significance of the ideal photoanode configuration for high-efficiency solar cells application.

© 2015 Published by Elsevier Ltd.

1. Introduction

Dye-sensitized solar cells (DSSCs), a promising alternative for the development of a new generation of photovoltaic devices, have advantages of simple fabrication procedures, low manufacturing cost and high theoretical efficiency [1–4]. A typical DSSC consists of dye-sensitized TiO₂ film, an electrolyte containing a suitable redox-couple and a Pt coated counter electrode [5,6]. Except the widely investigated TiO₂ photoanode [7–10], many researches on other alternative metal oxides such as ZnO, Cu₂O and SnO₂ have

been conducted [11–16]. Among these, SnO₂ has a higher electron mobility (100–200 cm² · V⁻¹ · s⁻¹) than TiO₂ (0.1–1 cm² · V⁻¹ · s⁻¹) indicating a faster diffusion transport of photoinduced electrons in SnO₂ than in TiO₂. Furthermore, SnO₂ has a larger band gap (3.8 eV) than TiO₂ (3.2 eV), which means DSSCs containing SnO₂ will be less sensitive to UV degradation, thereby improving long-term stability of cells. Because metal oxides with larger band gap can effectively suppress large number of oxidative holes in the valence band under UV illumination which has adverse effects on the performance of organic dyes and electrolytes [17]. However, a 300 mV positive shift of the conduction-band edge of SnO₂ with respect to that of TiO₂ will result in faster interfacial electron recombination and lower trapping density, as well as less adsorption of the dyes with acidic carboxyl groups due to the

* Corresponding author.

E-mail address: luyg@jlu.edu.cn (G. Lu).

lower isoelectric point [18,19]. Until now, the power conversion efficiency (PCE) of SnO₂ based devices still lingers around 5–6% [20–23], and is not comparable with that of TiO₂ based devices at all.

Hierarchical nanostructured materials are becoming more and more interesting in DSSCs, because they have many advantages such as sufficient dye loading, strong light scattering and fast electron transport [24,25]. According to literature, SnO₂ hollow sphere (SHS) based DSSCs have obtained PCE over 5%, which is mainly because of the better light-harvesting efficiency, faster charge extraction and reduced interfacial recombination [26]. Hence, hierarchical nanostructured SnO₂ is indispensable for achieving high-performanced photoanode. On the other hand, to combine the advantageous features of SnO₂ and TiO₂, various SnO₂/TiO₂ composite nanomaterials also have been synthesized and exhibit interesting photovoltaic performance in DSSCs application [27–29].

In our recent work, we present two kinds of SnO₂/TiO₂ composite materials: porous SnO₂/TiO₂ material (PSTM) and SnO₂@TiO₂ hollow sphere (STHS), both of which are applied in DSSCs and exhibit enhanced performance than P25 based cell. The PSTM is prepared by a facile and operable hydrothermal strategy. The interface and transient properties studied by electrochemical impedance spectroscopy (EIS) show fast electron transport and low recombination rate of PSTM based cell. Nitrogen adsorption isotherm analysis also indicates that the obtained hierarchical PSTM has an extraordinary specific surface area (151.1 m² g⁻¹). By using SiO₂ microspheres as the template, the macroporous STHS with diameter of 300 nm can be achieved. With enhanced light-scattering capability and electron-capture efficiency, the DSSC based on STHS photoelectrode shows a comparable PCE (5.82%) to that of P25 (5.33%). Finally, we fabricate DSSCs assembled using the double-layered photoanode with PSTM as the bottom layer and STHS as the top layer, which will ensure the amount of dye adsorption, offer fast electron transport and increase the path length of incident light in films for better light utilization. The PSTM+STHS based DSSC generates a large enhancement in short-circuit current density (17.49 mA cm⁻²) compared with the single-layered PSTM photoanode (14.86 mA cm⁻²), and thus an excellent PCE of 7.79%.

2. Experiments

2.1. Synthesis of the PSTM

All starting chemicals were analytical grade and used without further purification. PSTM was prepared by one-step hydrothermal process. Typically, 20 mg of the commercial TiO₂ powder (Degussa P25) was dispersed in 30 ml of precursor aqueous solution consisting of 0.65 g SnCl₂·2H₂O and 0.57 g NaF, followed by hydrothermal treatment at 180 °C for 24 h in a Teflon-lined autoclave. The product was collected by centrifuge and washed with absolute ethyl alcohol and deionized water three times, respectively. At last, the obtained sample was dried at 80 °C overnight and subsequently annealed at 550 °C for 2 h. The amount of P25 added to precursor solution was decided by the results obtained from the previous work (see Fig. S1 and Table S1).

2.2. Synthesis of the STHS

The STHS was synthesised by a facile water bath method. Firstly, monodisperse SiO₂ sphere templates with average diameter of ~245 nm were synthesized using a modified Stöber method [30]. Then, SnO₂ was deposited on the SiO₂ sphere templates by a sol-gel method to obtain SiO₂@SnO₂ core-shell structure. Typically, 0.8 g K₂SnO₃·3H₂O and 0.15 g SiO₂ samples were dispersed in the

mixed solution consisting of 50 mL deionized water and 25 mL ethyl alcohol. The mixture was placed in the water bath at 60 °C for 1 h with continuous stirring. The SHS was achieved by treating the as-prepared SiO₂@SnO₂ powder with 30 mL of 2 M NaOH aqueous solution at 50 °C for 1 h. In order to obtain STHS, 0.1 g SHS was dispersed in a mixture of 0.56 mL TiCl₄, 100 mL deionized water and 1 mL HCl (36 wt.%) by 30 min water bath at 80 °C. The temperature greatly affected the coating of the TiO₂ nanoparticles on SHS, and 80 °C is an optimum growth temperature in this study, as shown in Fig. S2. Subsequently, the product was collected by centrifuge and washed with absolute ethyl alcohol and deionized water three times, respectively. After dried at 80 °C for 8 h, the STHS was annealed at 550 °C for 1 h with a heating rate of 2 °C min⁻¹ in air. The synthesis procedure of the STHS is illustrated in Fig. 1.

2.3. Fabrication of the DSSCs

For comparison, we prepared three kinds of viscous paste based on P25, PSTM and STHS, respectively [31]. The coating of the as-prepared paste onto the clear FTO was done via the doctor blade method. The films were dried at 120 °C for 15 min, and subsequently annealed at 450 °C for 30 min in air. After cooling down to 80 °C, the films were immersed into a 0.4 mM dye solution (dye: N-719, solvent: t-butanol and acet-onitrile mixture with volume ratio of 1: 1) for 24 h at room temperature to load with dye. Finally, the DSSCs were constructed by a Pt-coated FTO counter electrode, I⁻/I³⁻ electrolyte and photoanode films using a vacuum back-filled method.

2.4. Characterization and photoelectrochemical measurement

The microstructure and morphology of the samples were characterized by scanning electron microscopy (SEM, JEOL JSM-7500F) and transmission electron microscopy (TEM, JEOL EM-2100). The crystallographic properties were evaluated by X-ray diffraction (XRD; Rigaku TTRIII, with Cu Kα1 radiation). The specific surface area was measured using a Micromeritics Gemini VII apparatus (Surface Area and Porosity System) based on the Brunauer–Emmett–Teller (BET) equation. The diffuse-reflectance spectra and absorbance of desorption dye from different anodes were performed on a Perkin-Elmer UV–vis spectrophotometer (SHIMADZU 2550). The current–voltage (I–V) characteristics of the DSSCs were measured by a Keithley 2400 Source Meter under a solar simulator (Newport, model: 94,023A, Xenon lamp, AM 1.5G, 100 mW cm⁻²). The incident photontocurrent efficiency (IPCE) spectra were measured as a function of wavelength from 400 to 800 nm with a spectral resolution of 5 nm on the basis of a Spectral Product Zolix DSC300PA. EIS was recorded using an electrochemical workstation (Solartron SI1287) at V_{oc} in the frequency range of

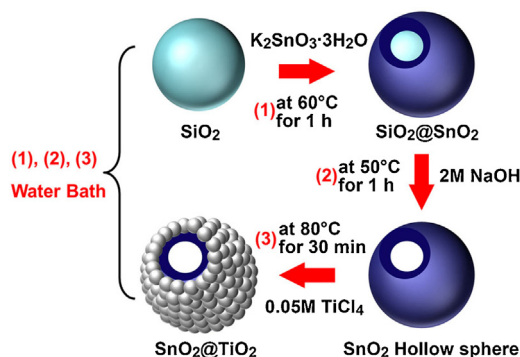


Fig. 1. Schematic illustration of the fabrication process of the STHS.

0.1–10⁶ Hz. The active area for solar cell performance test was set to 0.25 cm².

3. Results and discussion

3.1. Characterization of materials

The as-prepared and annealed samples were initially examined by XRD measurement. As shown in Fig. 2(a), Commercial TiO₂ (P25) is confirmed to be a mixture of anatase phase of TiO₂ (JCPDS no. 4-477) and rutile TiO₂ (JCPDS no. 76-1939). The XRD pattern of PSTM shows predominantly the formation of the SnO₂ phase while only the strongest peaks of TiO₂ are visible. Most of the diffraction peaks can be readily indexed to tetragonal cassiterite SnO₂ (JCPDS no. 41-1445), and it also clearly shows two relatively weak XRD peaks characteristic of anatase TiO₂ appeared at 2θ = 25.37 and 48.07 (JCPDS no. 4-477). Since the anatase phase is better than rutile and brookite for solar energy conversion, it is favorable for the preparation of TiO₂ particles to avoid the two phases, rutile and brookite. After annealing at 550 °C and removing SiO₂, the SHSs are crystallized into a single phase cassiterite SnO₂ (JCPDS no. 41-1445). All the peaks are broadened due to the nanocrystalline nature of the SnO₂ particles (Fig. 2(b)). It also identifies the STHS as a mixture of anatase phase of TiO₂ (JCPDS no. 4-477) and cassiterite SnO₂ (JCPDS 41-1445). No other oxides were detected, indicating the high purity of the obtained products.

Fig. 3 shows the low-temperature N₂ adsorption-desorption isotherms of PSTM and STHS. The inset provides the BJH adsorption average pore diameters of the two samples (PSTM=39.7 nm, STHS=63.2 nm), which are mainly in the mesoporous region. The Brunauer–Emmett–Teller (BET) specific surface area of the PSTM and STHS are determined as 151.1 and 94.9 m² g⁻¹, respectively, which are much larger than the conventional P25

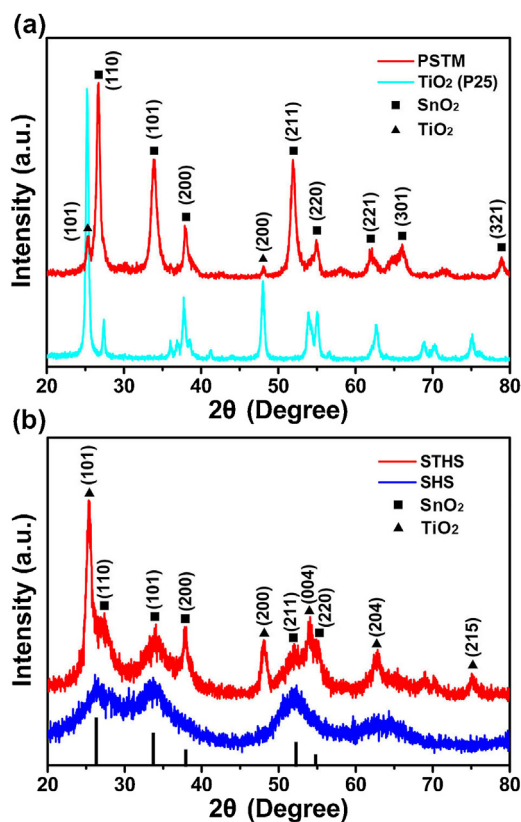


Fig. 2. XRD patterns of the PSTM and STHS samples.

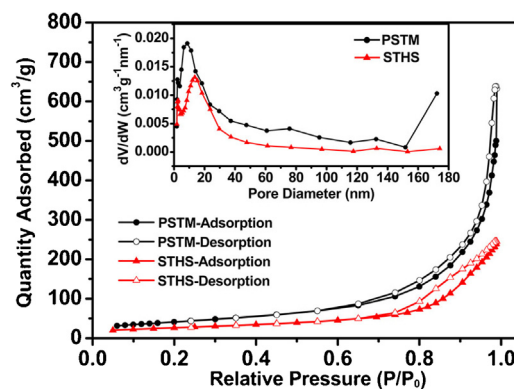


Fig. 3. N₂ adsorption-desorption isotherms of PSTM and STHS. Inset: corresponding BJH adsorption pore size distribution.

(50 ± 15 m² g⁻¹). This guarantees a larger amount of dye adsorption while enhancing the light harvesting of the photoanode simultaneously.

Fig. 4(a) shows the SEM observations on the surface of PSTM samples, indicating that the nanoporous material consists of SnO₂ nanosheets (SNSs) and TiO₂ nanoparticles (TNPs). The SNSs grow with overlapping and clustering, which can lead to the occurrence of abundant mesopores. Fig. 4(b) shows that the TNPs have good electrical connection with SNSs, resulting in fast electron diffusion from TiO₂ to SnO₂, a desired feature for DSSCs applications. The HRTEM image of TNP (Fig. 4(c)) reveals its polycrystalline nature, which coincides with the XRD measurement. Fig. 4(d) clearly shows that the interplanar spacing of ~0.26 nm and ~0.33 nm of a single SNS correspond to the (101) and (110) lattice planes of tetragonal cassiterite SnO₂ phase, respectively, by which the SNS can be identified to grow along (101) direction.

The surface morphology of SiO₂ template, SHS and STHS was characterized by SEM and provided in Fig. 5 (a), (b) and (c), respectively. SEM results indicate that the SiO₂ has uniform size of ~245 nm (Fig. 5 (a)). After using the NaOH aqueous solution to remove the SiO₂ sphere template, the SHS with a diameter ~255 nm is observed. Fig. 5(c) shows that the TiO₂ nanocrystal-coated SHSs exhibit good interconnection with each other by TNPs, which is beneficial for electron transport between the adjacent STHSs [32]. The inset of Fig. 5(c) clearly shows that the diameter of the STHSs increases to ~300 nm, and their macroscopic porous morphology is obtained. Fig. 5(d) provides the internal morphology (inset (i), (ii)) and crystal structure of the STHS. Inset (i) and (ii) reveal the hollow structure of STHS with TiO₂ spherical shell of ~25 nm in thickness. The TiO₂ nanocrystal exhibits interplanar spacing of ~0.24 nm, ~0.35 nm and ~0.23 nm that can be indexed as (004), (101) and (112) plane, respectively, as shown in Fig. 5(d), indicating good crystallinity of TiO₂ spherical shell.

3.2. Photovoltaic performance

To obtain an insight into the photovoltaic performance of PSTM and STHS, four types of nanoporous film (I) P25, (II) PSTM, (III) STHS, (IV) PSTM + STHS with similar thicknesses were prepared by doctor blade method on the FTO (Fig. 6). Film (IV) was double-layer constructed by ~3.3 μm of PSTM and ~3.6 μm of STHS. The thickness of electrodes was controlled by the number of coating times, showing a similar value of ~7 μm. After dye loading, all photoelectrodes were tested under an illumination of one sun condition (AM 1.5G, 100 mW cm⁻²). The photocurrent density voltage (J–V) curves and corresponding IPCE spectra for the DSSCs based on the four films (Cell (I): Film (I), Cell (II): Film (II), Cell (III): Film (III), Cell (IV): Film (IV)) are given in Fig. 7, and the

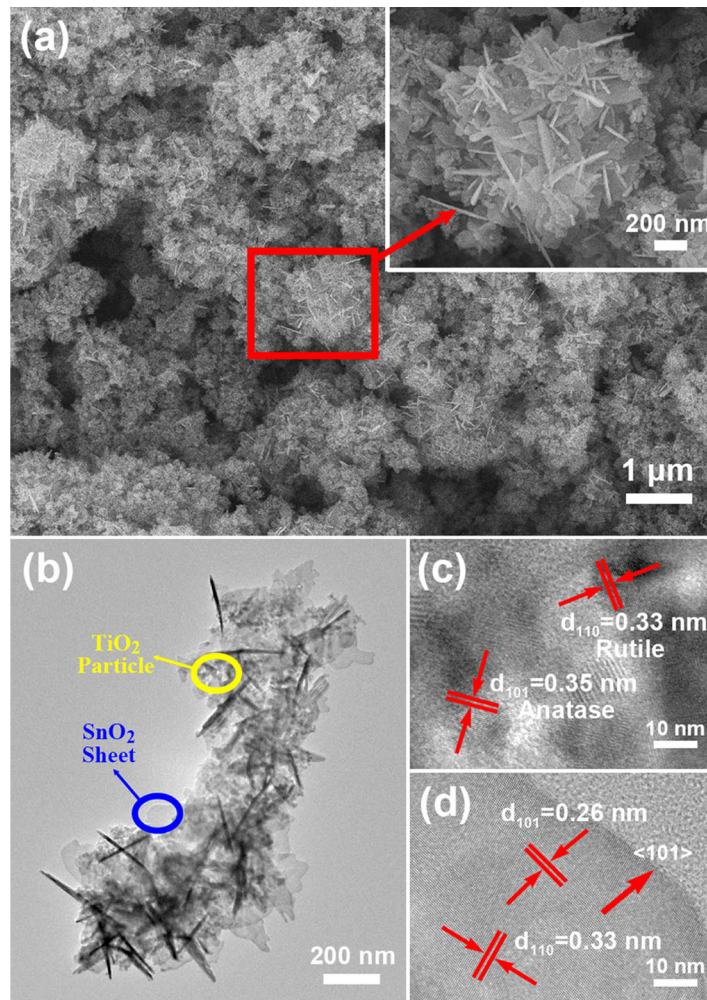


Fig. 4. SEM (a), TEM (b), and HRTEM (c, d) images of the PSTM. Inset of (a) shows a close inspection of the nanosheet cluster structure.

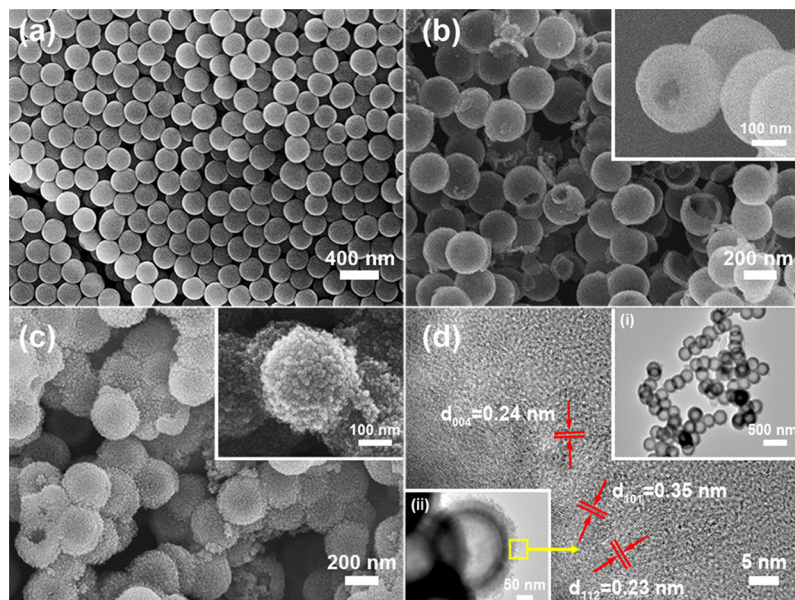


Fig. 5. SEM images of (a) SiO₂, (b) SHS, and (c) STHS. TEM, HR-TEM, and SAED images of (d) STHS.

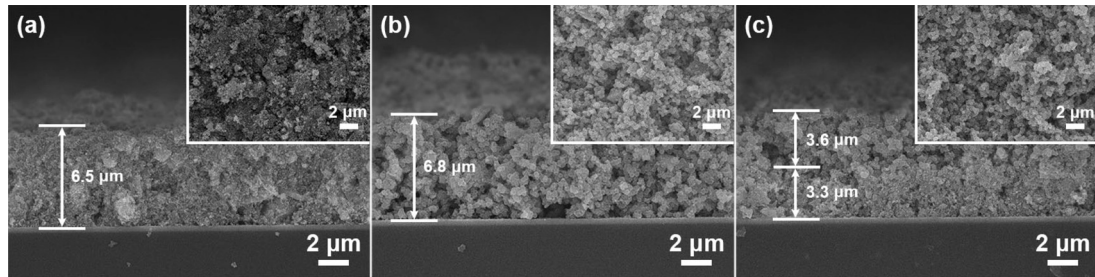


Fig. 6. Cross-section SEM images of the sintered (a) PSTM, (b) STHS and (c) PSTM+STHS films. Insets are the corresponding surface images of these films.

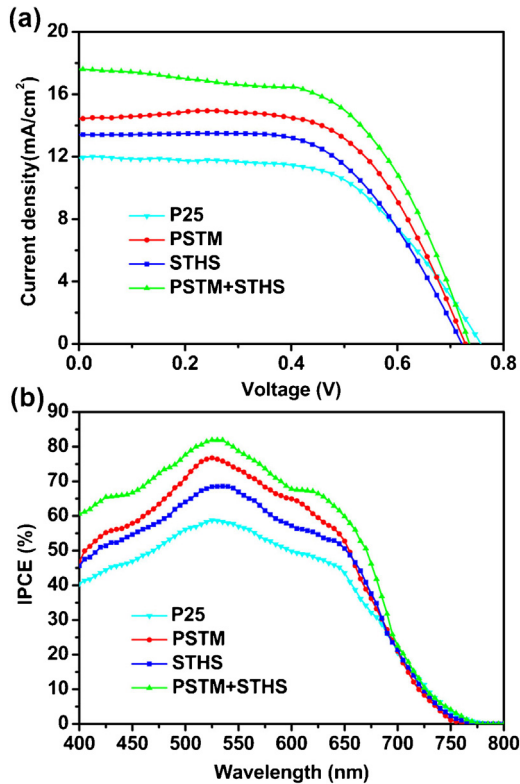


Fig. 7. (a) J–V curves and (b) IPCE spectra of DSSCs with photoelectrode films composed of P25, PSTM, STHS, and PSTM+STHS, respectively.

photovoltaic parameters derived from the J–V curves are summarized in Table 1.

As shown in Fig. 7(a) and Table 1, the short-circuit current density (J_{sc}) and the fill factor (FF) of Cell (II), Cell (III) and Cell (IV) are enhanced compared with that of Cell (I). Fig. 8 shows the energy band diagram for the PSTM and STHS based DSSCs, explaining the higher J_{sc} than conventional pure TiO_2 based DSSC. Because of the energy barrier of approximately 300 mV created by the TiO_2 layer, once the electrons are injected from the dye to TiO_2 and further to SnO_2 , they will have fewer chances to recombine with the electrolyte, resulting in improved electron collection

efficiency. On the other hand, because of the lower conduction band energy level of SnO_2 , there is an obvious decrease in their open-circuit photovoltage (V_{oc}). It is noteworthy that Cell (IV) exhibits the largest J_{sc} of 17.49 mA cm^{-2} and the highest PCE of 7.79% among the four cells tested. The significantly improved photocurrent than Cell (II) and Cell (III) may be due to its special photoanode structure in which the bottom and top layers are the as-prepared PSTM and STHS, respectively (Fig. 9 (a)). In particular, the STHS with porous shell and high surface area allows for light-scattering events and incident light trapping from multiscattering effect inside the STHS (Fig. 9 (b)), thus improving the light-harvesting efficiency. In addition, the PSTM bottom layer is designed to adsorb more dye and provide efficient electron transfer paths. The electrons injected from TiO_2 to SnO_2 can transport faster in SnO_2 due to its higher electron mobility than TiO_2 , leading to enhanced photocurrent (Fig. 9 (c)).

Fig. 7(b) presents the IPCE of the four cells, which are measured in the wavelength range of 400 to 800 nm. The IPCE results are in good agreement with the observation from Fig. 7(a). Both Cell (II) and Cell (III) show a significant increment of IPCE than Cell (I), which can be ascribed to the contribution of the relatively superior specific surface area and fast electron transport of PSTM and STHS, enabling the enhanced charge collection efficiency. Furthermore, Cell (IV) obtains a maximum IPCE as high as 82% at 525 nm (the peak of the N719 adsorption spectrum) due to the contribution of STHS scattering layer in the DSSC.

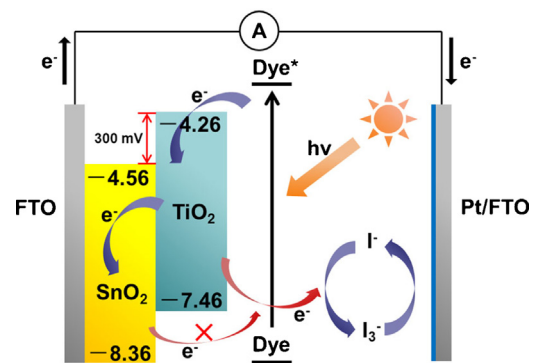


Fig. 8. Schematic diagrams for illustrating the energy band structure and electron transfer in the SnO_2/TiO_2 heterostructure.

Table 1

Average photovoltaic data of four different photoanodes, measured under one sun illumination ($AM\ 1.5\ G\ 100\ mW\ cm^{-2}$) and simulative value of resistance (R_1 , R_2 , and R_3) from EIS spectra calculated by equivalent circuit as shown in Fig. 11.

DSSCs	J_{sc} ($mA\ cm^{-2}$)	V_{oc} (V)	FF (%)	η (%)	R_1 (Ω)	R_2 (Ω)	R_3 (Ω)	dye adsorbed ($\times 10^{-7}$ mol cm^{-2})
Cell(I)	11.93 ± 0.08	0.76 ± 0.01	59 ± 1	5.33 ± 0.05	25.8	8.7	31.1	1.56 ± 0.11
Cell(II)	14.86 ± 0.15	0.73 ± 0.01	63 ± 1	6.80 ± 0.07	23.1	8.9	87.0	1.95 ± 0.23
Cell(III)	13.13 ± 0.16	0.72 ± 0.01	61 ± 1	5.82 ± 0.05	25.9	8.7	25.6	1.63 ± 0.15
Cell(IV)	17.49 ± 0.19	0.73 ± 0.01	61 ± 1	7.79 ± 0.05	26.1	8.6	61.5	1.72 ± 0.20

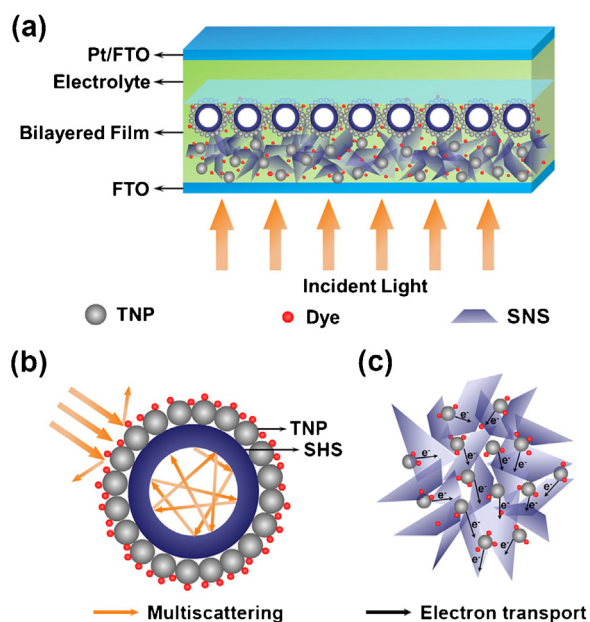


Fig. 9. (a) Typical cell structure diagram and the photoanode based on bilayered film. Illustration of (b) internal light multiscattering effect of the SHS, and (c) electron transport in the PSTM.

In order to have better understanding about the light-harvesting properties of the four bare electrode films, diffuse reflectance spectra and UV–vis absorption spectra were measured. Fig. 10 (a) reveals that the Film (III) and Film (IV) exhibit much strong reflectance in the visible light wavelength region (400–800 nm), even after the dye loading process (Fig. 10(b)), which means the STHS are very suitable as the light-scattering layer. These results

provide direct evidence for the analysis of Fig. 9(b). On the contrary, Film (I) and Film (II) exhibit relatively weak scattering effect due to the smaller pore size than the wavelength of visible light. Fig. 10(c) shows the Film (II) has the highest light absorption while the Film (IV) shows better light absorption ability than Film (II) and Film (III), which is mainly ascribed to the excellent dye adsorption ability of PSTM. Fig. 10(d) shows the absorption spectra of solutions of dyes desorbed from the films, the specific dye adsorption amount of films are presented in Table 1. Film (IV) benefits from the abundant dye adsorption for obtaining enough light absorption which will contribute to the enhancement of the J_{sc} . In addition, Film (III) and Film (I) have almost the same amount of dye adsorption, however, Film (III) shows a much better light-harvesting capability than Film (I) in the wavelength range of 400–800 nm, which can be explained by the incident light trapping effect inside the STHS (Fig. 9 (b)).

EIS analysis was used to investigate the charge transport and recombination in DSSCs. Measurement was taken at V_{oc} in the dark, and the frequency range was from 0.1 Hz to 10^6 Hz [33,34]. The inset of Fig. 11(a) illustrates the equivalent circuit simulated to fit the impedance spectra, and the electrochemical parameters derived from Z-view software are summarized in Table 1. Apparently, the four kinds of cells have similar values of R_1 and R_2 , denoting the lumped series resistance of cells and the charge transfer resistance at the electrolyte/Pt/FTO interface at high frequency, respectively, which is because of the same cell structure and Pt/FTO counter electrode. As can be seen from Fig. 11(a), the larger semicircle at intermediate frequency is attributed to charge recombination resistance at the semiconductor/dye/electrolyte interface (R_3) [35], which is vital for the photovoltaic performance. It is noteworthy that Cell (II) shows the largest R_3 , indicating the slowest charge recombination in the PSTM film. Cell (III) has a much smaller semicircle, implying much electron recombination

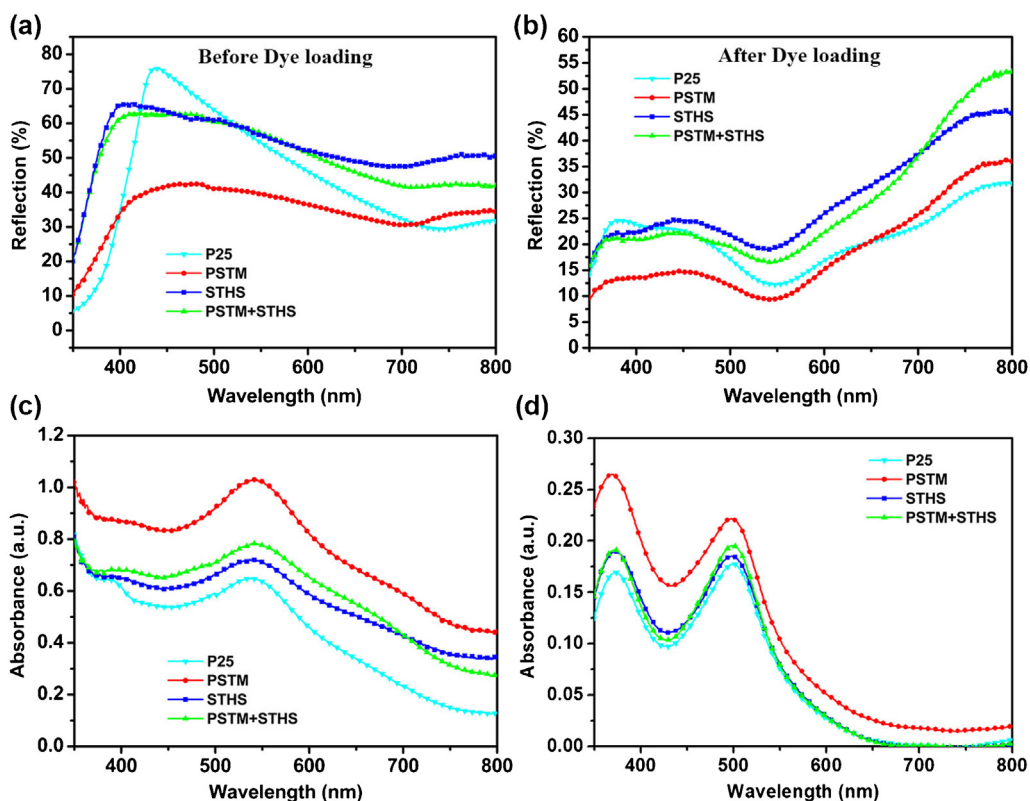


Fig. 10. Diffuse reflectance spectra of the four photoanode films (a) before and (b) after the dye loading process. UV–vis absorption spectra of (c) the photoanode films loaded dye and (d) the solutions of dyes that were desorbed from the films, respectively.

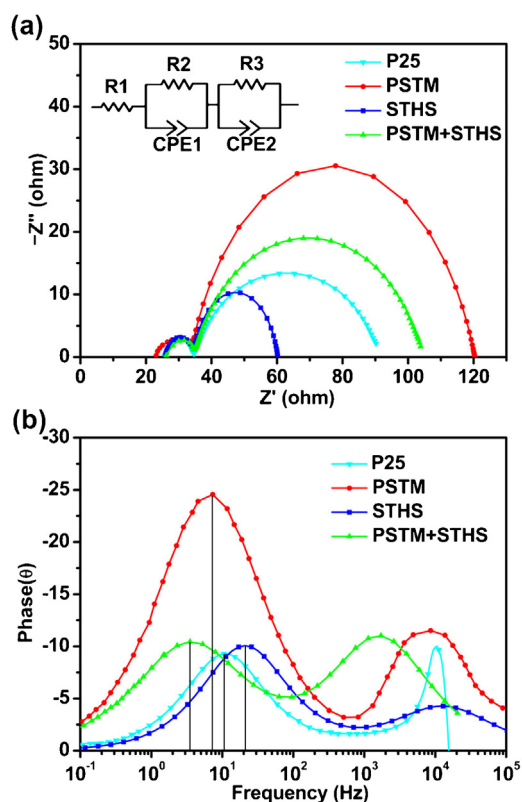


Fig. 11. (a) Nyquist plots, and (b) corresponding Bode-phase plots from EIS measurement for fabricated DSSCs using P25, PSTM, STHS, and PSTM+STHS electrodes.

losses to electrolyte, which is common for cells based on SHS. This coincides with the J–V results, and can be ascribed to the indirect connection among SHSs suppressing the electron transfer process. The electron lifetime (τ_e) in the oxide film can be estimated according to the relation $\tau_e = 1/2\pi f_{\max}$, where f_{\max} is the maximum frequency of the mid-frequency peak. From the Bode-phase plots shown in Fig. 11(b), the f_{\max} values for Cell (I), Cell (II), Cell (III) and Cell (IV) are estimated to be 10.8, 7.3, 20.9 and 3.5 Hz, respectively. Although Cell (IV) has a smaller R_3 than Cell (II), the electron lifetime of Cell (IV) (45.5 ms) is longer than that of latter (21.8 ms) due to the larger chemical capacitance for the Cell (II). Therefore, we can conclude that the engineered enhanced electron injection promotes the electron transfer and charge collection efficiency, accordingly, better photovoltaic performance will present for Cell (IV) (see Fig. 7).

4. Conclusions

In summary, one-step hydrothermal route has been developed to synthesize PSTM which has large specific surface area, fast electron transport, and slow charge recombination. The PCE for PSTM based cell is up to 6.80%, increased by 27.6% compared to bare P25 based cell (5.33%). We also demonstrate a facile water bath approach to prepare STHS. Though the shorter electron lifetime for the STHS photoanode ascribed from the faster interfacial electron recombination, the PCE of DSSC based on STHS (5.82%) is higher than that of P25 because of the higher dye loading and superior light scattering ability. However, this kind of hierarchical SHS-TiO₂ still show some disadvantages compared with other work [36]. The correlation table is presented in Table S2, so there is still much further research to do. In addition, the DSSC based on bilayered photoelectrode (3.3 μm PSTM + 3.6 μm STHS)

exhibits an impressive power conversion of 7.79%, indicating a 14.6% improvement compared to the single layered PSTM photoelectrode (6.80%) with the same thickness of 6.5 μm due to the longer electron lifetime and superior light scattering ability for the former. Hence, we consider that the strategy of engineered integration of different composite materials opens up many exciting opportunities to improve the performance of existing metal oxide photoanode systems and have good potential for other applications such as Li-ion battery, solid-state electrolyte-based DSSCs and quantum dot-sensitized solar cells.

Acknowledgements

This work was supported by National Nature Science Foundation of China (Nos. 61374218, 61134010, and 61327804) and Program for Chang Jiang Scholars and Innovative Research Team in University (No. IRT13018), National High-Tech Research and Development Program of China (863 Program, No. 2013AA030902 and 2014AA06A505) and the project development plan of science and technology of Jilin Province (20130521009JH).

Appendix A. Supplementary data

Supplementary data associated with this article can be found, in the online version, at <http://dx.doi.org/10.1016/j.electacta.2015.07.102>.

Notes and references

- [1] B. O'Regan, M. Grätzel, *Nature* 353 (1991) 737.
- [2] A. Yella, H.W. Lee, H.N. Tsao, C.Y. Yi, A.K. Chandiran, M.K. Nazeeruddin, E.W.G. Diau, C.Y. Yeh, S.M. Zakeeruddin, M. Grätzel, *Science* 334 (2011) 629.
- [3] H. Lee, D. Hwang, S.M. Jo, D. Kim, Y. Seo, D.Y. Kim, *ACS Appl. Mater. Interfaces* 4 (2012) 3308.
- [4] Y.P. Liu, S.R. Wang, Z.Q. Shan, X.G. Li, J.H. Tian, Y.M. Mei, H.M. Ma, K.L. Zhu, *Electrochim. Acta* 60 (2012) 422.
- [5] N.G. Park, J.V. Lagemaat, A.J. Frank, *J. Phys. Chem. B* 104 (2000) 8989.
- [6] J.Y. Liao, J.W. He, H. Xu, D.B. Kuang, C.Y. Su, *J. Mater. Chem.* 22 (2012) 7910.
- [7] S. Ito, P. Chen, P. Comte, M.K. Nazeeruddin, P. Liska, P. Péchy, M. Grätzel, *Prog. Photovoltaics Res. Appl.* 15 (2007) 603.
- [8] M. Fujimoto, T. Kado, W. Takashima, K. Kaneto, S. Hayase, *J. Electrochem. Soc.* 153 (2006) A826.
- [9] D.H. Wang, H. Lee, S.Y. Jang, S.M. Jo, D. Kim, Y. Seo, D.Y. Kim, *ACS Appl. Mater. Interfaces* 3 (2011) 2719.
- [10] Y. Zhang, L. Wu, E. Xie, H. Duan, W. Han, J. Zhao, *J. Power Sources* 189 (2009) 1256.
- [11] J.S. Bendall, L. Etgar, S.C. Tan, N. Cai, P. Wang, S.M. Zakeeruddin, M. Grätzel, M.E. Welland, *Energy Environ. Sci.* 4 (2011) 2903.
- [12] C. Magne, T. Moehl, M. Urien, M. Grätzel, T.J. Pauporté, *Mater. Chem. A* 1 (2013) 2079.
- [13] Q.F. Zhang, T.P. Chou, B. Russo, S.A. Jenekhe, G.Z. Cao, *Angew. Chem., Int. Ed.* 47 (2008) 2402.
- [14] Y.F. Wang, J.W. Li, Y.F. Hou, X.Y. Yu, C.Y. Su, D.B. Kuang, *Chem. Eur. J.* 16 (2010) 8620.
- [15] Y.F. Wang, K.N. Li, C.L. Liang, Y.F. Hou, C.Y. Su, D.B. Kuang, *J. Mater. Chem.* 22 (2012) 21495.
- [16] E. Ramasamy, J. Lee, *J. Phys. Chem. C* 114 (22) (2010) 032.
- [17] A. Thapa, J. Zai, H. Elbohy, P. Poudel, N. Adhikari, X.F. Qian, Q.Q. Qiao, *Nano Research* 7 (2014) 1154.
- [18] V. Ganapathy, B. Karunakaran, S.W. Rhee, *J. Power Sources* 195 (2010) 5138.
- [19] C.T. Gao, X.D. Li, X.P. Zhu, L.L. Chen, Z.M. Zhang, Y.Q. Wang, Z.X. Zhang, H.G. Duan, E.Q. Xie, *Journal of Power Sources* 264 (2014) 15.
- [20] K.N. Li, Y.F. Wang, Y.F. Xu, H.Y. Chen, C.Y. Su, D.B. Kuang, *Appl. Mater. Interfaces* 5 (2013) 5105.
- [21] S. Gubbala, H.B. Russell, H. Shah, B. Deb, J. Jasinski, H. Rypkema, M.K. Sunkara, *Energy Environ. Sci.* 2 (2009) 1302.
- [22] J. Chen, C. Li, F. Xu, Y.D. Zhou, W. Lei, L.T. Sun, Y. Zhang, *RSC Advances* 2 (2012) 7384.
- [23] W. Tian, C. Zhang, T.Y. Zhai, S.L. Li, X. Wang, M.Y. Liao, K. Tsukagoshi, D. Golberg, Y. Bando, *Chem. Commun.* 49 (2013) 3739.
- [24] G. Shang, J. Wu, S. Tang, M. Huang, Z. Lan, Y. Li, J. Zhao, X. Zhang, *J. Mater. Chem.* 22 (25) (2012) 335.
- [25] Z. Teddy, T. Uddin, Y. Nicolas, C. Olivier, T. Toupance, C. Labrugère, L. Hirsch, *ACS Appl. Mater. Interfaces* 3 (2011) 1485.
- [26] N. Tétéreault, É. Arseneault, L. Heiniger, N. Soheilnia, J. Brilliet, T. Moehl, S. Zakeeruddin, G.A. Ozin, M. Grätzel, *Nano Lett.* 11 (2011) 4579.

- [27] C. Gao, X. Li, B. Lu, L. Chen, Y. Wang, F. Teng, J. Wang, Z. Zhang, X. Pan, E. Xie, *Nanoscale* 4 (2012) 3475.
- [28] G. Shang, J. Wu, M. Huang, J. Lin, Z. Lan, Y. Huang, L. Fan, *J. Phys. Chem. C* 116 (20) (2012) 140.
- [29] C.L. Wang, J.Y. Liao, Y.B. Zhao, A. Manthiram, *Chem. Commun.* 51 (2015) 2848.
- [30] Z.W. Zhang, Y.M. Zhou, Y.W. Zhang, X.L. Sheng, S.J. Zhou, S.M. Xiang, *Appl. Surf. Sci.* 286 (2013) 344.
- [31] P.L. Zhao, P.F. Cheng, B. Wang, S.T. Yao, P. Sun, F.M. Liu, J. Zheng, G.Y. Lu, *RSC Adv.* 4 (64) (2014) 737.
- [32] S.R. Gajjela, C. Yap, P. Balaya, *J. Mater. Chem.* 22 (10) (2012) 873.
- [33] Q. Wang, S. Ito, M. Grätzel, F.F. Santiago, I.M. Ser (r), J. Bisquert, T. Bessho, H. Imai, *J. Phys. Chem. B* 110 (25) (2006) 210.
- [34] R. Buonsanti, E. Carlino, C. Giannini, D. Altamura, L.D. Marco, R. Giannuzzi, M. Manca, G. Gigli, P.D. Cozzoli, *J. Am. Chem. Soc.* 133 (2011) 19216.
- [35] W. Ho, J.C. Yu, J. Yu, *Langmuir* 21 (2005) 3486.
- [36] S.H. Ahn, D.J. Kim, W.S. Chi, J.H. Kim, *Adv. Funct. Mater.* 24 (2014) 5037.